

# 1 High Altitude Echoes from the Equatorial Topside 2 Ionosphere during Solar Minimum

3 **S. Derghazarian, D. L. Hysell, K. Kuyeng and M. A. Milla**

4 <sup>1,2</sup>Earth and Atmospheric Sciences, Cornell University, Ithaca, New York, USA

5 <sup>2,3</sup>Jicamarca Radio Observatory, Lima, Peru

## 6 **Key Points:**

- 7 • High altitude echoes observed in the topside ionosphere over Jicamarca at post-
- 8      midnight times during solar minimum
- 9      • The echoes inhabit altitudes between 1000–2200 km
- 10     • High altitude echoes exhibit spectral sidebands at the lower-hybrid frequency

11 **Abstract**

12 We describe a new class of nonthermal plasma density irregularities observed in the post-  
 13 midnight topside equatorial ionosphere under low solar flux conditions. They are distinct  
 14 from irregularities associated with equatorial spread *F* (ESF) in terms of their morphol-  
 15 ogy and because they exhibit strong spectral sidebands at the lower-hybrid frequency.  
 16 The coherent echoes were observed in a series high-altitude radar experiments performed  
 17 at Jicamarca utilizing long- and coded double-pulse modes and a dual-beam mode. The  
 18 coded double-pulse mode was used to measure the low-frequency characteristics of the  
 19 echoes with fine range resolution. Doppler shifts of the main backscatter line were ob-  
 20 served to fall between  $\pm 150$  m/s. The long-pulse mode was employed for high-frequency  
 21 spectral analysis which revealed the presence of strong spectral sidelobes at the lower-  
 22 hybrid frequency. A dual-beam mode was used to investigate the horizontal structure  
 23 of the echoes. Zonal drift speeds of 50-70 m/s were inferred with this mode, and longi-  
 24 tudinal dimensions of approximately 270 km were estimated. The paper summarizes with  
 25 a discussion of different mechanisms that may be responsible for the phenomenon and  
 26 the lower-hybrid sidebands in particular.

27 **1 Introduction**

28 Plasma density irregularities in the upper atmosphere have been studied extensively  
 29 using radio and radar techniques since the dawn of the space age. When caused by ther-  
 30 mal fluctuations in a plasma in equilibrium, these irregularities form the basis of inco-  
 31 herent scatter radar (ISR) techniques [Farley et al., 1961]. However, when the irreg-  
 32 larities are due to nonthermal effects, much stronger (e.g. up to seven orders of magni-  
 33 tude in case of ESF [Farley et al., 1970] ) coherent scatter may be observed. Sources of  
 34 coherent scatter at the magnetic equator include electron density irregularities driven  
 35 by neutral turbulence in the mesosphere [Rastogi and Bowhill, 1976], irregularities driven  
 36 by gradient drift [Rogister and D'Angelo, 1970; Sudan et al., 1973] and Farley-Buneman  
 37 instabilities [Farley 1963; Buneman 1963] in the equatorial electrojet [Forbes, 1981], and  
 38 the so-called 150-km echoes [Balsley, 1964; Kudeki and Fawcett, 1993; Chau and Kudeki,  
 39 2006; Chau et al., 2013] in the equatorial valley region thought to be related to the upper-  
 40 hybrid instability [Lehmacher et al., 2020; Longley et al., 2020]. In the postsunset equa-  
 41 torial *F* region, equatorial spread *F* (ESF) [Booker and Wells, 1938; Hysell et al., 2000;  
 42 Woodman., 2009] is a commonplace phenomenon characterized by plasma irregularities

43 with scale sizes ranging from centimeters to several hundreds of kilometers and altitudes  
 44 that can reach up to about 1500 km [Farley et al., 1970] during quiet periods and higher  
 45 during geomagnetic storms .

46 Coherent echoes from even higher altitudes above 1500 km in the inner plasmas-  
 47 phere were discovered recently by accident when they contaminated noise samples in high-  
 48 altitude ISR data [Hysell et al., 2019]. The echoes took the form of thin layers rather  
 49 than convective plumes and occurred mainly in the predawn sector. Unlike coherent scatter  
 50 associated with ESF which occurs at all solar flux levels, these high-altitude echoes  
 51 have been observed only during low solar-flux conditions. Most significantly, we will show  
 52 that the high-altitude echoes in question exhibit strong sidebands at the lower-hybrid  
 53 frequency for protons. They thus constitute a new phenomenon.

54 In this paper, we present findings from a series of dedicated radar experiments run  
 55 during the fall and spring of 2018 and 2019 to probe the high-altitude echoes. The spa-  
 56 tial, temporal and spectral characteristics of the echoes will be described and evaluated.  
 57 Subsequently, we discuss some well known irregularities and instabilities associated with  
 58 the production of lower hybrid waves and evaluate their relevance for our observations.  
 59 These include Lower Hybrid Solitary Structures (LHSS), VLF mode conversion, and lower  
 60 hybrid drift instability. Finally, we conclude with a summary of our findings and plans  
 61 for future experiments.

## 62 **2 Experimental Methodology and Results**

63 Figure 1 shows observations of the high-altitude scattering layers made on Sept.  
 64 19–20, 2018. The observations were made with a double-pulse mode. Each pulse in the  
 65 pair employed a 13-bit Barker code with a baud width of 100  $\mu$ s. The lag between pulses  
 66 was 4 ms. This is several times longer than the correlation time for incoherent scatter  
 67 at 50 MHz. A single circular polarization was used for transmission. Sampling was per-  
 68 formed at 50  $\mu$ s intervals, and the incoherent integration time was 15 s. The double-pulse  
 69 coherence was calculated from the modulus of the normalized autocorrelation function  
 70 at the 4-ms lag. Noise removal was not performed in the normalization, and so the co-  
 71 herence is a measure both of the correlation time of the echoes and the signal-to-noise  
 72 ratio [Farley, 1969]. The coherence gives a visual representation of the distribution of the  
 73 irregularities in range and time.

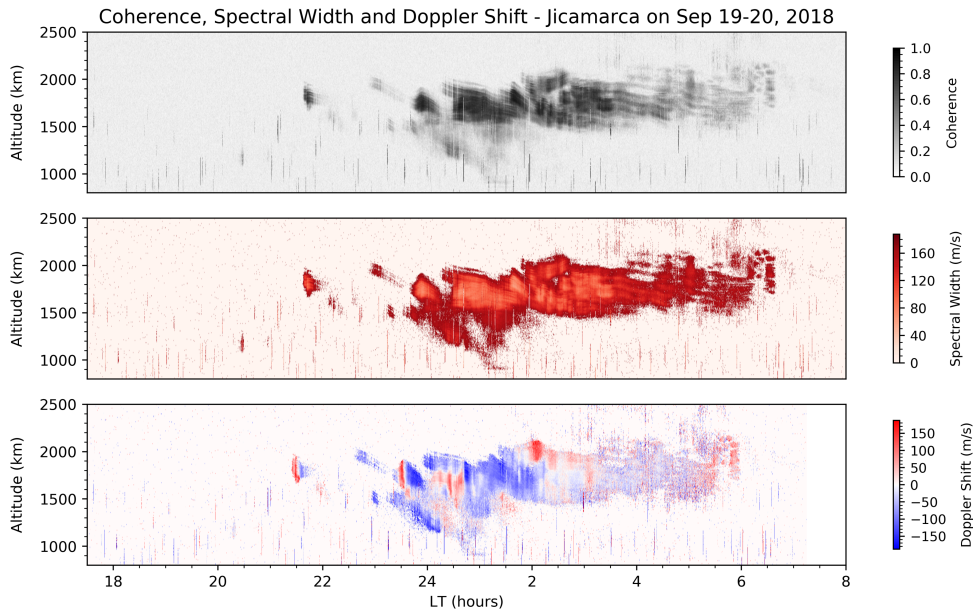


Figure 1: Examples of high-altitude scattering layers. The upper panel indicates coherence, the middle panel spectral width, and the lower panel line-of-sight Doppler shift. Short lived echoes in the bottom half of the panels are due to space debris which has not been removed.

74 The echoes presented first as small patches, intermittently spaced in range and time,  
 75 followed by a much larger structure that spanned altitudes between 1000–2200 km, ap-  
 76 pearing shortly before midnight and persisting significantly until local sunrise at ground  
 77 level ( $\approx$  0600 LT). Considerable fine structure was present in the backscatter at times.  
 78 Horizontal streaks were evident for the last few hours of the event. This could well be  
 79 an indication of structures drifting slowly through the radar beam and persisting for a  
 80 long duration rather than layers per se.

81 The Doppler shifts and spectral widths shown in the second and third panels in  
 82 Figure 1 were derived from the phase and modulus of the normalized correlation func-  
 83 tion, respectively, this time including noise subtraction in the normalization such that  
 84 the results are independent of the signal-to-noise ratio.

85 Doppler velocities were roughly consistent with range rates and varied from -150  
 86 m/s to 150 m/s. The largest Doppler shifts and sharpest variations in range and time  
 87 occurred around midnight. Variations in the Doppler shift were partially but imperfectly  
 88 correlated with variations in intensity. Spectral widths were as small as about 40 m/s  
 89 in the most intense regions of backscatter and increased in the peripheral regions.

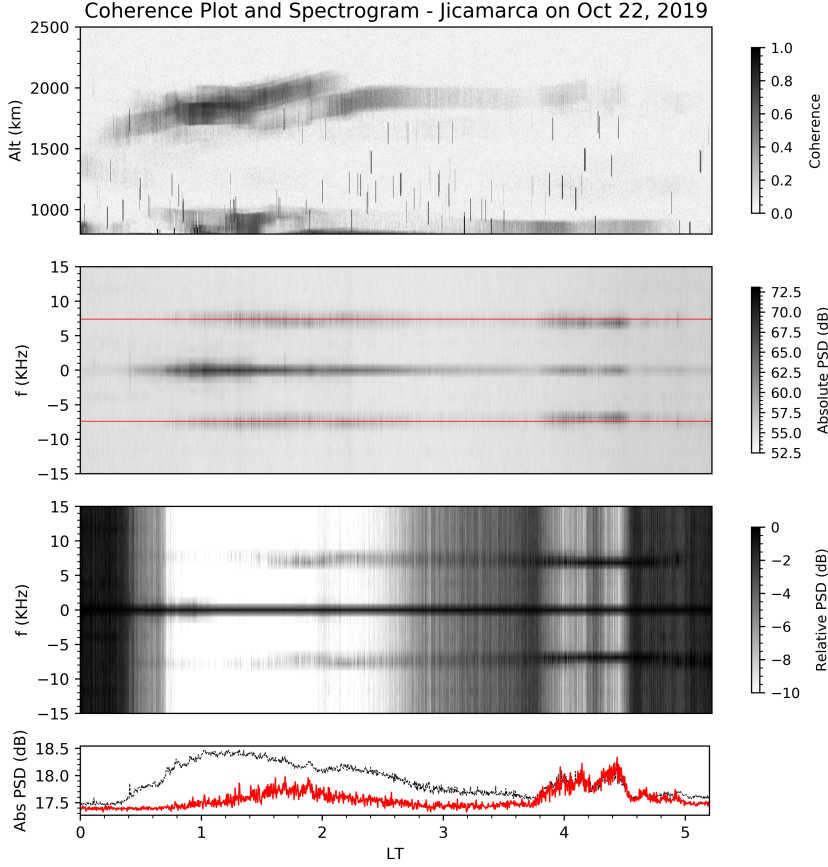


Figure 2: High-altitude echoes received from a 2-ms long pulse experiment conducted on Oct 22, 2019. Echoes appear predominantly between 0000-0300 LT. Altitudes ranged from 1200–2000 km. The top panel shows the coherence. The middle and lower panels depict non normalized and normalized spectrograms, respectively, for altitudes near  $\approx 1800\text{km}$  (see text). The lower panel displays normalized line plots of the zero frequency bin (shown in black) and the 6.8 - 7.8 KHz bin (shown in red) respectively, indicating the level of correlation between both signals in the spectrogram. The horizontal red lines (7.4KHz) superimposed on the spectrograms denote the theoretical value of the lower hybrid frequency, calculated from the warm plasma dispersion relation (see Equation 4 in Appendix), at an altitude of 1800km for typical densities and temperatures present around midnight. The densities and temperatures used were modeled by SAMI2-PE (Varney et al. [2012])

90 Figure 2 shows several hours of post-midnight observations made on Oct 22, 2019.  
 91 For this experiment, a single long pulse with a 2-ms pulse width and a 40-ms IPP was

92 used. Samples were acquired at  $1\ \mu\text{s}$  intervals. For analysis comparable to that applied  
 93 to the September data, we applied a filter with a  $100\ \mu\text{s}$  boxcar impulse response func-  
 94 tion prior to detection. The coherence was calculated using an  $800\ \mu\text{s}$  lag time. The range  
 95 resolution of the experiment was relatively poor compared to the previous one.

96 The October echoes can be observed to extend from midnight to approximately lo-  
 97 cal sunrise time (0540 LT). Several prominent scattering layers can be seen centered at  
 98  $\approx 1700\text{km}$ ,  $1800\text{ km}$  and  $1900\text{km}$  in Figure 2, and at  $1400\text{km}$  and  $1500\text{km}$  in Figure 4.  
 99 Echoes from equatorial spread *F* (ESF) were visible at lower altitudes, but they were not  
 100 obviously related to the high-altitude structures even though they overlapped in time.  
 101 The poor range resolution of the experiment prevents the detection of fine structure in  
 102 the layers.

103 The long-pulse mode permits the calculation of broadband Doppler spectra. We  
 104 have found only interference at frequencies outside the band between  $\pm 15\ \text{kHz}$  and so  
 105 concentrate here on frequencies within this band. The two lower panels in Figure 2 show  
 106 spectrograms constructed from samples corresponding to the upper scattering layer at  
 107  $1800\text{-km}$  range. The incoherent integration time used here was  $15\ \text{s}$ . The center panel  
 108 shows absolute power spectral density on an arbitrary scale, and the bottom panel shows  
 109 the relative power spectral density normalized to the power in the zero-frequency bin.

110 The most important features in Figure 2 are the prominent sidebands at Doppler  
 111 shifts equal to the lower hybrid frequency for protons, about  $6\text{--}9\ \text{kHz}$  depending on the  
 112 altitude and ambient density, for the entire duration of the echoes. In the center panel,  
 113 the  $6.8\text{ -- }7.8\ \text{KHz}$  bin, corresponding to the range of lower hybrid frequencies at  $\approx 1800\text{km}$   
 114 is most prominent. Higher frequency ( $7.8\text{ -- }8.8\ \text{KHz}$ ) and lower frequency ( $5.8\text{ -- }6.8\ \text{KHz}$ )  
 115 bins are also present. The highest frequency bin decreases in intensity from midnight to  
 116 4LT, while the middle and lowest frequency bin increase in intensity as would be expected  
 117 by the drop in ambient densities from post-midnight to early morning hours. The same  
 118 result was obtained when samples were taken from the lower scattering layer centered  
 119 at  $1400\text{ km}$  in Figure 4, with the spectrogram in that case showing slightly higher fre-  
 120 quency sidebands consistent with the larger magnetic flux density at lower altitudes (see,  
 121 e.g., lower two panels of Figure 4).

122 It is noteworthy also that the ratio of the power in the sidebands to the power in  
 123 the zero-frequency bin is not constant. For example, the enhancement in the sidebands

124 between about 0350 – 0430 LT occurred at a time when the overall scattering intensity  
 125 was diminishing and the layer was dissipating.

126 Furthermore, an exploded view of a portion of the bottom panel in Figure 2, shown  
 127 in Figure 3, reveals yet another interesting characteristic of the emissions – that of sig-  
 128 nificant, persistent fluctuations in amplitude. A comparison of these fluctuations in the  
 129 lower hybrid sidebands to those in the zero frequency bins (not shown here) shows that  
 130 they are synchronized, demonstrating the fact that the fluctuations are not a form of en-  
 131 hanced hybrid lines in the incoherent scatter spectrum.

132 The characteristic frequency derived from the homogeneous lower hybrid disper-  
 133 sion relation (as shown in Appendix A) was superimposed onto the spectrogram in Fig-  
 134 ure 2 using a thin red line. To arrive at this frequency, we used magnetic field intensity  
 135 values from IGRF-13, assumed a nighttime electron density value consistent with mea-  
 136 surements shown in Hysell et al. [2017a], and selected a nominal temperature of 1000  
 137 K. Employing the homogeneous approximation to calculate the characteristic frequency  
 138 is justifiable to the extent the influence of plasma inhomogeneities on wave propagation  
 139 and instability is small [Treumann and Baumjohann, 1997].

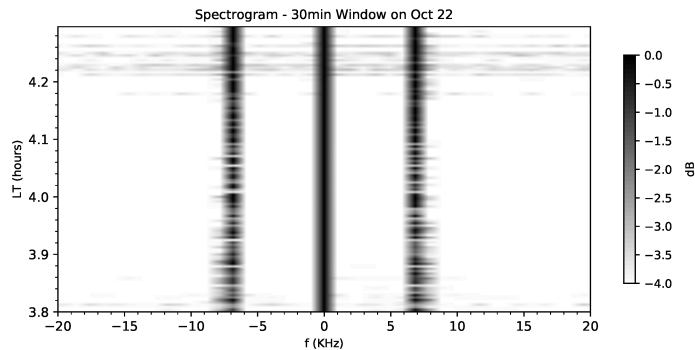


Figure 3: Exploded spectrogram for times between 0348–0412 LT and  $\approx 1800$  km. Dramatic intensity variations of the lower hybrid waves in time can be seen.

140 Dual-beam experiments were conducted on Oct 23 and 24, 2019, to infer the zonal  
 141 drifts and zonal extent of the high-altitude scattering regions. The two beams used or-  
 142 thogonal linear polarizations. Beams A and B were pointed westward and eastward, re-  
 143 spectively, with a separation of about  $1.5^\circ$  or by a little more than two individual beamwidths.  
 144 The magnetic declination of the pointing positions was about the same for each beam  
 145 (see Figure 6).

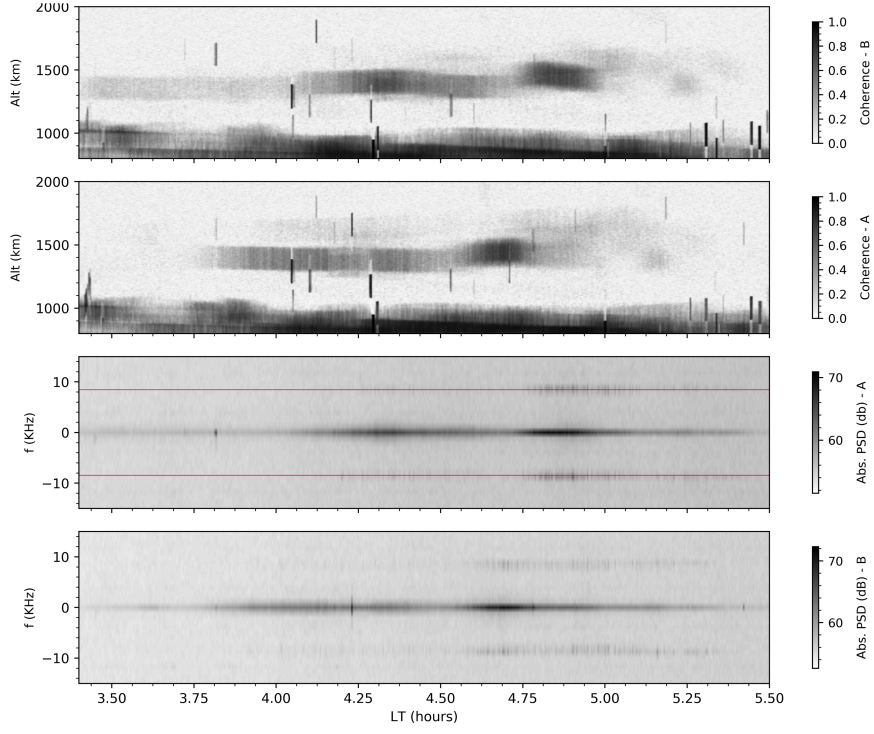


Figure 4: Coherence of echoes from dual-beam experiments conducted on Oct 23, 2019.

Transmitters A (westward) and B (eastward) point to different scattering volumes separated zonally by  $\approx 1.5^\circ$ . The lower two panels depict non normalized spectrograms for altitudes near  $\approx 1400\text{km}$  (see text). The horizontal red lines (8.4KHz) superimposed on the spectrogram in the third panel denote the theoretical value of the lower hybrid frequency, calculated from the warm plasma dispersion relation (see Equation 4 in Appendix), at an altitude of 1400km and for typical densities and temperatures present around 4.5 LT. The densities and temperatures used were modeled by SAMI2-PE (Varney et al. [2012])

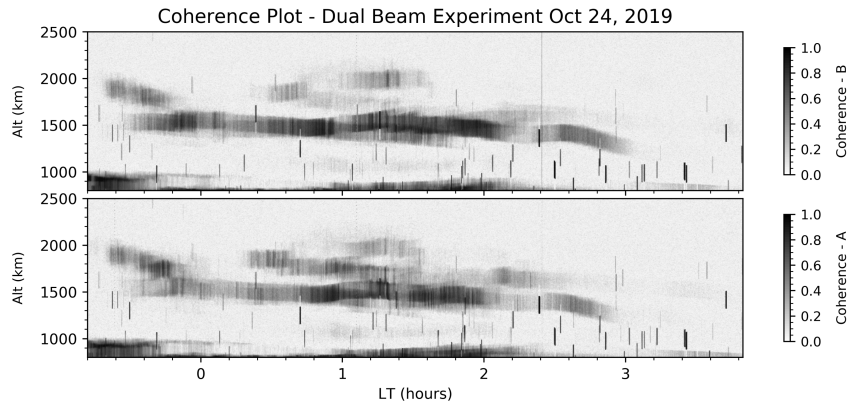


Figure 5: Echoes from dual-beam experiments conducted on Oct 23 - 24, 2019.

146 On Oct. 23, 2019, the echoes ranged from just 1200–1500 km altitude. To estimate  
 147 drifts, we measured the shift in time of apparently common features in the two upper  
 148 panels of Figure 4. The region with the highest coherence appeared in the westward-pointing  
 149 beam approximately 15 min. before appearing in the eastward-pointing beam. This was  
 150 also the region with the strongest lower-hybrid lines. The zonal distance between the po-  
 151 sitions where the layer intersected the two antenna beams was about 35 km – 40 km. These  
 152 figures imply a zonal drift speed of about 45 – 50 m/s eastward.

153 On Oct. 24, 2019, as shown in Figure 5, the echoes were more spread in altitude.  
 154 Between 0100–0130 LT, three different height ranges were occupied by scatterers: 1200  
 155 – 1500 km, 1500 – 1700 km, and 1750 - 2000 km. In contrast to the previous day, many  
 156 of the features appear nearly identical in both beams, while others appear to be drift-  
 157 ing eastward at about 70 m/s. The data are fairly ambiguous, however, and the appar-  
 158 ent motion of the scatterers only approximates the true motion to the extent that the  
 159 scatterers evolve slowly. On both Oct. 23 and 24, 2019, the coherence measured with  
 160 beams A and B exhibited similar if shifted features. This suggests that the underlying  
 161 structure evolved with relatively long timescales.

162 The longitudinal dimensions of the scattering structures can be estimated by mul-  
 163 tiplying the average drift speed by the duration of the echoes observed in either one of  
 164 the beams. To simplify the analysis, we consider only the experiment on Oct. 23, 2019,  
 165 when the totality of the structure appeared to be drifting eastward at a uniform speed.  
 166 In this case, the longitudinal extent can be estimated to be about 270 km.

### 167 **3 Overview of Ionospheric Processes Associated with Lower Hybrid 168 Waves**

169 The discovery of lower hybrid waves in the topside post-midnight equatorial iono-  
 170 sphere/ inner plasmasphere prompts a review of other regions and contexts in geospace  
 171 where lower hybrid waves play significant roles. Several relevant observations and lines  
 172 of inquiry are described below.

#### 173 **3.1 Lower Hybrid Solitary Structures (LHSS)**

174 LHSS's are axisymmetric and spatially localized structures elongated along mag-  
 175 netic field lines and having perpendicular dimensions that vary from a few to several ther-

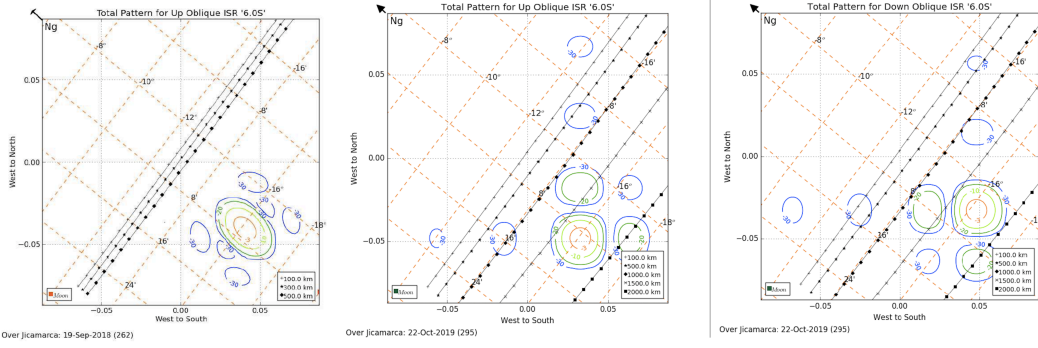


Figure 6: The leftmost panel shows the transmitter main lobe and sidelobe positions for the Barker coded double pulse experiment on Sept 19 - 20, 2018. The center and right panels show the main lobe and sidelobe positions for the westward and eastward transmitters respectively, used in the dual beam experiments on Oct 23 and 24, 2019. An angle of  $\approx 1.5^\circ$  separates them. The configuration for the long pulse experiment with a single pointing position is not shown in this figure but is similar to the leftmost panel.

176      mal ion gyroradii (10-100 m at auroral latitudes) [Schuck et al., 2003]. They are char-  
 177      acterized by large amplitude bursts of lower hybrid electrostatic waves having frequen-  
 178      cies slightly above and below the lower hybrid resonance [Schuck et al., 1998]. They re-  
 179      side within density depletions that vary from a few percent to several tens of percent of  
 180      the background electron density [Knudsen et al., 1998; McAdams et al., 1998] and found  
 181      to exhibit a Gaussian density profile [Hoymork et al., 2001]. They are frequently observed  
 182      at auroral latitudes. The first definite observations of LHSS's were made by the MARIE  
 183      sounding rocket [Lebelle et al., 1986]. It was found that the peak electric field associated  
 184      with the structures was several times larger than the background VLF hiss. In auroral  
 185      regions, LHSS's were observed by the Freja satellite at altitudes ranging from 1450 – 1750  
 186      km [Dovner et al. 1994; Eriksson et al., 1994]. Both satellite and sounding rocket data  
 187      have revealed that LHSS's always appear whenever VLF hiss is present [Dovner et al.,  
 188      1997; Lynch et al., 1999].

189      Currently, two classes of theories are applied to LHSS's: linear and non-linear. The  
 190      nonlinear treatments center on modulational instability, lower hybrid collapse, and strong  
 191      turbulence. The first treatment is based on the parametric instability of a lower hybrid

192 pump wave to low frequency density fluctuations in a homogeneous plasma in which the  
 193 density fluctuations are assumed to be triggered by a modulational instability [Chang,  
 194 Shapiro et al., 1993]. The pump wave follows a homogeneous lower hybrid disper-  
 195 sion relation, and the instability of the wave results in its decay into other lower hybrid  
 196 waves and lower frequency density fluctuations [Shukla et al; 1994]. However, a study  
 197 by Pécseli et al. [1996] eliminates the possibility of this instability being the driving mech-  
 198 anism in LHSS's by demonstrating that LHSS's are not spaced at regular intervals as  
 199 predicted by the modulational instability but follow a Poisson distribution. The second  
 200 treatment, lower hybrid collapse, rests on the assumption that the density depletions and  
 201 lower hybrid waves are both related to a parallel electron ponderomotive force produced  
 202 by a high frequency electron  $E \times B$  drift [Musher and Stermann, 1975a; Musher and Stermann,  
 203 1975b; Shapiro et al., 1993]. Statistical studies comparing the collapse theory with  
 204 Freja satellite data, however, have shown that this theory is also incompatible with ex-  
 205 perimental data [Pécseli et al., 1996]. Robinson [1999] attempted to rectify these discrep-  
 206 ancies of the collapse theory by resorting to the theory of strong turbulence which as-  
 207 sumes a four phase nucleation cycle that includes nucleation, collapse, arrest and relax-  
 208 ation [Doolen et al., 1985; Robinson et al., 1996; Robinson et al., 1999]. However, a sta-  
 209 tistical study of LHSS's in the auroral ionosphere performed by Schuck et al. [2002] does  
 210 not support this theory.

211 The linear class of theories explain the production of lower hybrid waves in LHSS's  
 212 by mode conversion of VLF auroral hiss to lower hybrid eigenmodes of preexisting den-  
 213 sity depletions through linear scattering off of density irregularities [Pinçon et al., 1997;  
 214 Schuck et al., 1998; Schuck et al. , 1999a and Schuck et al. , 1999b]. Previous studies  
 215 [Titova et al., 1984; Inan and Bell 1985; Bell and Ngo, 1988] presented satellite data show-  
 216 ing that lower hybrid waves are commonly stimulated by VLF whistlers interacting with  
 217 field aligned density irregularities with wavelengths of the order of the lower hybrid waves.  
 218 The dispersive properties of the eigenmodes are then modified by the inclusion of the  
 219 Hall current generated by the  $E \times B$  drift which accounts for most of the spectral char-  
 220 acteristics of LHSS's observed experimentally [Schuck et al., 2003]. No diamagnetic cur-  
 221 rents or drift waves are needed despite the assumption of plasma inhomogeneity [Schuck  
 222 et al., 1998]. Studies by Seyler et al. [1994] and Schuck et al. [1998] explain LHSS's with  
 223 linear theory applied to an inhomogeneous cold plasma composed of pre-existing cylin-  
 224 drical density depletions. The cylindrical nature of the density depletions motivates the

choice of cylindrical basis functions, decomposing the lower hybrid waves into right and left hand rotating modes relative to the magnetic field. A consequence of this theory is wave solutions that consist of a continuous spectrum of waves above the lower hybrid resonance (LHR) outside the density depletions of the LHSS's and a discrete spectrum of waves below the LHR inside the density depletions. The predictions of linear theory generally agree with interferometric [Bonnell et al., 1998] and spectral analyses [Pécseli et al., 1996; Pécseli et al., 1997; Kjus et al., 1998] of the electric fields within the structures.

In addition to the assumptions of linear theory, there is every reason to believe that azimuthal ion currents within density depletions also participate in the excitation of lower hybrid waves. Ions are presumed to play a role in the instabilities because of numerous observations by sounding rockets [Vago et al., 1992 ; Lynch et al., 1996] in which TAI (Transversely Accelerated Ions) were found with higher energies inside LHSS's as compared to the general background values. Data from TOPAZ-III has in fact revealed direct correlations between TAI's, enhanced electric field fluctuations and density depletions in thousands of LHSS's [Arnoldy et al., 1992]. The contribution of the ion current to the excitation of lower hybrid waves in LHSS's was investigated by Vakim et al. [1997]. The study found that an azimuthal ion current in a density cavity could lead to a positive growth rate through the Cherenkov interaction of resonant ions with the waves. The cavity considered was radially inhomogeneous and followed a Gaussian density profile. Chibisov [2012] and Aarenkov et al. [2019] investigated the special case of a radially inhomogeneous ion ring distribution within a homogeneous plasma. They also found that when certain conditions were met, an instability was triggered, leading to the growth of lower hybrid waves.

In studies by Malingre et al. [2008] and Berthelier et al. [2008], LHSS's were found for the first time at equatorial latitudes. They were discovered following the detection of lower hybrid waves by the DEMETER satellite at equatorial latitudes in large scale, deep density depletions spanning several hundreds of km longitudinally and with densities two to three orders of magnitude lower than that of the surrounding plasma. These emissions were associated with bursts of thermal ions, narrowband electromagnetic ELF waves and shown to evolve into large amplitude quasi-monochromatic wave packets that bore resemblance to those observed in LHSS's at auroral latitudes. The scale length of the irregularities contained within depletions were found to be 10 m across and 40 m along

258 the field lines when  $\Delta n_i/n_i \approx 10\%$ . Berthelier et al. [2008] found the phenomena in  
 259 the nighttime ionosphere between 2000 – 2300 LT and both studies indicated that the  
 260 density depletions were associated with periods of disturbance in the geomagnetic field.  
 261 The experimental data suggested that the interaction of the depletions with whistlers  
 262 generated through tropospheric lightning discharges below the orbital path of the satel-  
 263 lite was the source of the lower hybrid emissions.

264 The similarities observed between auroral and equatorial LHSS's suggest they both  
 265 share the same underlying physics. In both cases they are observed in regions of strong  
 266 VLF noise and in underdense plasmas ( $\omega_{pe} < \omega_{ce}$ ). However, the energy source of the  
 267 background hiss present at equatorial latitudes is very different from that responsible  
 268 for auroral hiss, with the former presumed to be caused by energetic electrons [Kintner.,  
 269 1991] and the latter by lightning generated whistlers. A unique feature of the equato-  
 270 rial LHSS's is the presence of narrowband ELF.

271 Similarly to the earlier studies in auroral regions and mid-latitudes, Berthelier et  
 272 al. [2008] highlighted two possible mechanisms for the excitation of lower hybrid waves  
 273 in equatorial density depletions. The first is a linear process involving mode conversion  
 274 of electromagnetic whistlers scattering off of pre-existing density depletions. The second  
 275 mechanism is through a parametric instability in which the density depletions and lower  
 276 hybrid waves are generated concurrently [Lee et al., 1984]. The electric field measure-  
 277 ments in Malingre et al.[2008] however, do not support the non-linear explanation.

### 278 3.2 Lower Hybrid Drift Instability

279 Another possible mechanism for the generation of the echoes is a lower hybrid drift  
 280 instability. Temperature and/or density gradients in an inhomogeneous plasma give rise  
 281 to a diamagnetic drift which couples with a drift wave leading to an instability through  
 282 inverse Landau damping [Huba et al., 1981]. To arrive at an expression for the growth  
 283 rate of the instability, perturbed quantities were assumed to vary linearly, the analysis  
 284 was restricted to electrostatic phenomena where  $\beta \ll 1$  ( $\beta = 8nT/B^2$ ), and only  
 285 oscillations perpendicular to  $B$  were considered. A fundamental requirement for the in-  
 286 stability is that electrons be magnetized and ions unmagnetized. Thus, a simple expres-  
 287 sion for the ion demagnetization condition in a collisional plasma was given by  $\frac{\nu_{ii}}{\Omega_i} k^2 r_{Li}^2 \leq$   
 288 1 where  $r_{Li}$  denotes the ion gyroradius and  $\nu_{ii}$  the ion-ion collision frequency [Huba and

289 Ossakow, 1979a]. Ion-ion collisions, which appear in the  $\nu_{ii}$  term above, contribute to  
 290 the demagnetization process by pushing the ions across magnetic field lines, a crucial step  
 291 in exciting the instability through resonance with the perpendicular drift wave. They  
 292 also set a critical background density value. On the contrary, all other collisions (electron-  
 293 ion, electron-electron and electron-neutral), lead to a damping of the wave, setting an  
 294 upper threshold to the density scale length ( $L_n$ ) given by  $L_n < r_{Li}\sqrt{(kv_{thi}/\nu_e)}$ . The  
 295 ion demagnetization condition and scale length threshold are the two important param-  
 296 eters which determine the viability of the lower hybrid drift instability for specific irreg-  
 297 ularity wavelengths and altitudes. For the 0.36 m and 0.11 m irregularities seen by the  
 298 ALTAIR and Tradex radars on Kwajalein Atoll, the minimum densities required are  $2 \times$   
 299  $10^9 m^{-3}$  and  $2 \times 10^8 m^{-3}$  respectively. Thus, the lower hybrid drift instability is oper-  
 300 able at ranges where high altitude echoes at Jicamarca are observed. However, for the  
 301 3 m irregularities seen by Jicamarca, the minimum density required is  $> 10^{11} m^{-3}$ , in  
 302 addition to extremely sharp scale lengths of less than 15 m. Both of these conditions are  
 303 not satisfied at the topside or lower plasmaspheric altitudes above Jicamarca and lead  
 304 us to consider the possibility of other mechanisms, possibly remote coupling, working  
 305 in conjunction with the lower hybrid drift instability.

## 306 4 Discussion

307 The data presented in this preliminary study is insufficient to support a conclu-  
 308 sion regarding which of the processes reviewed in the previous section is responsible for  
 309 the high altitude irregularities observed over Jicamarca.

310 For example, to determine whether the structures can be categorized as LHSS's,  
 311 more detailed information about the longitudinal and field-aligned dimensions of the struc-  
 312 tures would be needed. This could be gathered, for example, using a fully steerable radar  
 313 like ALTAIR that could provide longitudinal mapping of the structures. Finer spatial  
 314 resolution is also necessary to accurately measure the transverse dimensions and deter-  
 315 mine whether the larger structures are a discontinuous collection of smaller ones with  
 316 dimensions characteristic of LHSS's. If further radar experiments prove that the high-  
 317 altitude echo phenomenon is ubiquitous, sun synchronous satellite data at the appropri-  
 318 ate altitudes could be useful for a statistical study of the dimensions of the echoes along  
 319 field lines and its electric field fluctuations.

320 Whether simple VLF mode conversion is taking place without all of the other as-  
 321 sociated characteristics of equatorial LHSS's is another hypothesis worth exploring. This  
 322 assumption cannot be discounted because not all studies provide conclusive evidence that  
 323 observed lower hybrid wave emissions from field aligned irregularities are indicative of  
 324 LHSS's. To verify this hypothesis we cannot use radar data alone since VLF hiss is pre-  
 325 dominantly electromagnetic whereas the radar can only observe electrostatic phenom-  
 326 ena. Simultaneous radar and sounding rocket experiments would be needed in order to  
 327 determine if a correlation exists between lower hybrid wave power and the presence of  
 328 background hiss. A spectral analysis of the hiss would further indicate whether it is lightning-  
 329 induced or the result of equatorial hiss [Morgan, 1979].

330 The direct involvement of a lower hybrid drift instability in the generation of 3-m  
 331 irregularities at Jicamarca was mainly discounted in the previous section. However, mea-  
 332 surements from higher frequency equatorial radars such as ALTAIR and Tradex could  
 333 shed light on whether a cross-scale coupling mechanism between the irregularities ex-  
 334 ists.

335 It is also interesting to note that gyrolines naturally present in the ISR spectra tend  
 336 towards the lower hybrid resonance when the aspect angle approaches zero. In a study  
 337 by Hysell et al. [2017], gyrolines were shown to appear in ISR spectra processed from  
 338 Arecibo data in the 100 - 200 km range interval. Whether these lines are also present  
 339 in the ISR spectra above Jicamarca, for aspect angles close to zero and for ranges where  
 340 the high altitude echoes are observed, would need to be examined. If this is the case, it  
 341 would suggest the possibility that the lower hybrid sidebands are an enhancement of the  
 342 lower hybrid line feature naturally present in the ISR spectra, by means of an instabil-  
 343 ity.

## 344 5 Summary and conclusions

345 We have presented data from experiments conducted to probe a new class of non-  
 346 thermal 3-m plasma density irregularities causing VHF radar echoes in the equatorial  
 347 topside/ inner plasmasphere, mainly in the postmidnight sector. The echoes were char-  
 348 acterized in terms of their gross morphology and low-frequency spectral moments. Their  
 349 characteristics were broadly similar to those of irregularities generated in the topside by  
 350 convective instability related to equatorial spread *F*. However, the echoes were also found

351 to exhibit strong sidebands at the lower hybrid frequency, something which has not been  
 352 observed before. It is unclear at this point whether the sidebands are an incidental fea-  
 353 ture of density irregularities which happen to form in the topside or a crucial component  
 354 of the process responsible for creating the irregularities in the first place.

355 Various well-known phenomena involving lower-hybrid waves in the ionosphere were  
 356 reviewed as possible candidates to help explain the irregularities. The most important  
 357 features of the irregularities observed are the following:

- 358 1. Irregularities appear in the predawn sector of the topside ionosphere and lower plas-  
 359 masphere and form structures that most often span altitudes in the range of 1500–  
 360 2200 km
- 361 2. Coherence varies throughout the structures, and the irregularities dissipate entirely  
 362 before local sunrise
- 363 3. Lower hybrid waves are present for the entire duration and range of altitudes where  
 364 the high altitude irregularities are observed, and were not detected within the ESF  
 365 present at lower altitudes. A very large increase in relative intensity was noted in  
 366 portions of the echoes between 0400–0500LT on Oct 22, 2019, where the lower hy-  
 367 brid sideband intensity became comparable to that of the zero frequency bin, even  
 368 as the structures had almost dissipated.
- 369 4. Only eastward zonal drifts were observed from 50m/s - 70 m/s
- 370 5. Zonal dimensions of several hundred km were calculated
- 371 6. Line of sight Doppler shifts vary from -150 m/s and 150 m/s and have been ob-  
 372 served to change orientation frequently within the structures present in the Septem-  
 373 ber 20 2018 postmidnight sector. More experiments are needed to determine whether  
 374 this phenomenon is commonplace. The Doppler shifts tracked the range rates of  
 375 the echoes.
- 376 7. Structures appear to be distinct from ESF but occur at similar post-midnight times.  
 377 The echoes only appear in patches shortly before midnight in contrast to ESF.

378 Additional experiments involving radar interferometry and imaging, long pulse codes  
 379 for overspread targets, bistatic measurements for inferring meridional drifts, aspect sen-  
 380 sitive experiments, and supporting in situ measurements are required for investigating  
 381 the irregularities further.

382 Radar interferometry and imaging [Hysell and Chau, 2006] can be used to visual-  
 383 ize fine structures within the scattering volume in three dimensions. The long and dou-  
 384 ible pulse experiments suffered from tremendous ambiguity with respect to the spatial  
 385 distribution of structures. Imagery in the meridional direction would yield an estimate  
 386 of the magnetic aspect sensitivity of the lower-hybrid lines.

387 Using long coded pulses, e.g. alternating codes, the lower-hybrid spectra could be  
 388 resolved finely in range. This would allow us to investigate the transverse structure and  
 389 dimensions of the lower-hybrid waves more finely. In addition, it would give us the abil-  
 390 ity to measure changes in the lower hybrid frequency due to the ambient density drop  
 391 from midnight to early morning local times. This could potentially be a novel method  
 392 for measuring densities at high altitudes in the post-midnight sector.

393 Radar measurements of bulk drifts and dimensions along field lines would give ad-  
 394 dditional information on the structures. In order to make this experiment possible, we would  
 395 need to use a bistatic or multistatic system such that the condition for field-aligned scat-  
 396 ter could be met at multiple points along a field line.

397 Additional experiments could be carried out using ALTAIR and Tradex to gain in-  
 398 formation about the irregularities at shorter wavelengths. This would prove important  
 399 for isolating the processes responsible for their generation. In addition, the echoes could  
 400 be mapped continuously in space using the steerability of these systems.

401 Our understanding of the structures can also be considerably improved by com-  
 402 paring radar data with that gained by satellites and sounding rockets. One of the lim-  
 403 itations of radar experiments is the need to compromise between spectral resolution and  
 404 range resolution. Both instruments can be used to gather more detailed spectral and elec-  
 405 tron density measurements. Sounding rockets especially can be launched simultaneously  
 406 during radar experiments and provide direct comparisons with radar data. Satellite con-  
 407 junctions are difficult to manage as a rule, but if the irregularities prove to be as ubiq-  
 408 uitous as they now seem, finding them could be practical.

409 Further investigation is needed to determine whether ESF conditions favor the emer-  
 410 gence of the high-altitude irregularities. Additional observations should be made dur-  
 411 ing June equinox when ESF conditions are relatively unlikely to occur in the Peruvian  
 412 sector.

413 Finally, numerical simulations of cross-scale coupling between irregularities of dif-  
 414 ferent wavelengths, and numerical verification of the existence and possibility of enhance-  
 415 ment of lower hybrid lines for the altitudes at which the irregularities in this study were  
 416 observed, will be explored in more detail in a subsequent manuscript.

417 *Acknowledgements* The Jicamarca Radio Observatory is a facility of the Insti-  
 418 tuto Geofísico del Perú operated with support from NSF award AGS-1732209 through  
 419 Cornell. The help of the staff is much appreciated. Data used for this publication are  
 420 available through the Madrigal database (see <http://www.openmadrigal.org.>), and found  
 421 under Jicamarca ISR experiments.

422 **Appendix**

423 **Dispersion Relation of Lower Hybrid Waves in Homogeneous Plasma**

424 In this section we derive an approximate dispersion relation for lower hybrid elec-  
 425 trostatic waves in a homogeneous plasma. We follow a similar procedure to the one used  
 426 in [Hysell et al., 2017b]. Since the dominant ion is  $H^+$  at the altitudes at which the echoes  
 427 were observed, i.e. from 1200 km to 2200 km, we simplify the analysis considerably by  
 428 assuming a two species plasma (electrons and  $H^+$ ). The expression for the cold plasma  
 429 lower hybrid resonance frequency given by Swanson [2003] is:

$$\omega_{LH}^2 = \omega_{ce}\omega_{ci} \left( \frac{\omega_{pe}^2 + \omega_{ce}\omega_{ci}}{\omega_{ce}^2 + \omega_{pe}^2} \right) \quad (1)$$

430 which includes a dependence on the magnetic field, electron density and ion species but  
 431 excludes kinetic effects. Since  $\Omega_i^2 \ll \omega^2 \ll \Omega_e^2$  at LH frequencies, we can treat the  
 432 ions as unmagnetized and the electrons as magnetized.

The longitudinal projection of the dielectric tensor (dielectric response function) is given by:

$$K = 1 + \frac{1}{k^2 \lambda_{de}^2} [1 + \sum_{n=-\infty}^{\infty} \frac{\omega}{\sqrt{2}k_{\parallel}v_{te}} \Lambda_n(\eta^2) Z(\Theta')] + \frac{1}{k^2 \lambda_{di}^2} [1 + \theta Z(\theta)] \quad (2)$$

433 where  $N$  is the number of ion species,  $\theta = \frac{\omega/k}{\sqrt{2}v_{th}}$  and  $\Theta' = \frac{\omega - n\Omega_e}{\sqrt{2}k_{\parallel}v_{te}}$  are the normal-  
 434 ized ion and electron velocities respectively,  $v_{te} = \sqrt{K_B T/m_e}$  is the thermal electron  
 435 velocity,  $\eta^2 = \frac{k_{\perp}^2 v_{te}^2}{\Omega_e^2}$ ,  $\cos^2 \beta = \frac{k_{\parallel}^2}{k^2}$  with  $\beta$  representing the angle between the  $k$  vector  
 436 and  $B$ , and  $Z$  is the plasma dispersion function. Note that the second term in the di-  
 437 electric response function is the electron susceptibility, and the last term is the ion sus-  
 438 ceptibility.

439 Using the large  $\Theta'$  approximation for  $Z(\Theta')$  (since  $k_{\parallel}v_{th} \ll \omega$ ):  $Z(\Theta') \approx i\sqrt{\pi}e^{-\Theta'^2} -$   
 440  $\Theta'^{-1}(1 + \frac{1}{2\Theta'^2} + \dots)$ , in conjunction with the expansion form of the modified Bessel func-  
 441 tion  $I_n(\eta^2)$  for small  $\eta^2$  (since  $k_{\perp}v_{th} \ll \Omega_e$ ):  $I_n(\eta^2) = (\frac{1}{2}\eta^2)^n \sum_{k=0}^{\infty} \frac{(\frac{1}{4}\eta^4)^k}{k!(n+k)!}$ , we can  
 442 rewrite a more simple approximation for the electron susceptibility. Since the  $n = 0$  term  
 443 is dominant in equation 2, to first approximation, the real part of the electron suscep-  
 444 tibility can be written as:

$$\begin{aligned} Re(\chi_e) &= \frac{1}{k^2\lambda_d^2} \left[ 1 - (1 - \eta^2 + \frac{3}{4}\eta^4 + \dots)(1 + \frac{k_{\parallel}^2 v_{te}^2}{\omega^2} + 3\frac{k_{\parallel}^4 v_{te}^4}{\omega^4} + \dots) \right] \\ &\approx \frac{\omega_{pe}^2}{\omega^2} \left[ \frac{\omega^2}{\Omega_e^2} - \cos^2 \beta \left( 1 + 3\frac{k_{\parallel}^2 v_{te}^2}{\omega_{LH}^2} \right) + \dots \right] \end{aligned}$$

445 where the  $\omega^4$  term was replaced by  $\omega^2\omega_{LH}^2$  with the help of equation 1. Following the  
 446 same procedure for the ion susceptibility and using the large angle approximation for  $Z(\theta)$ :

$$\begin{aligned} Re(\chi_i) &\approx \frac{\omega_{pi}^2}{k^2 v_{ti}^2} \left[ -\frac{k^2 v_{ti}^2}{\omega^2} - \frac{3k^4 v_{ti}^4}{\omega^2 \omega_{LH}^2} + \dots \right] \\ &\approx \frac{\omega_{pi}^2}{\omega^2} \left[ -1 - \frac{3k^2 v_{ti}^2}{\omega_{LH}^2} + \dots \right] \end{aligned}$$

447 Note that the parameters  $\frac{k_{\perp}^2 v_{te}^2}{\Omega_e^2}$ ,  $\frac{k_{\parallel}^2 v_{te}^2}{\omega^2}$ , and  $\left| \frac{k_{\parallel}}{k_{\perp}} \right|$  were only retained up to second order.  
 448 After combining the electron and ion susceptibilities into equation 2, the dielectric re-  
 449 sponse function becomes:

$$K \approx 1 + \frac{\omega_{pe}^2}{\omega^2} \left[ \frac{\omega^2}{\Omega_e^2} - \cos^2 \beta \left( 1 + 3\frac{k_{\parallel}^2 v_{te}^2}{\omega_{LH}^2} \right) \right] + \frac{\omega_{pi}^2}{\omega^2} \left[ -1 - \frac{3k^2 v_{ti}^2}{\omega_{LH}^2} \right] + \dots \quad (3)$$

450 The wave frequency can be derived by setting  $K = 0$ :

$$\omega_r^2 \approx \left[ \omega_{pi}^2 \left( 1 + \frac{3k^2 v_{ti}^2}{\Omega_e^2 \Omega_i^2} \right) + \omega_{pe}^2 \cos^2 \beta \left( 1 + 3\frac{k_{\parallel}^2 v_{te}^2}{\Omega_e^2 \Omega_i^2} \right) \right] / \left( 1 + \frac{\omega_{pe}^2}{\Omega_e^2} \right) \quad (4)$$

451 where we ignore the imaginary part since  $\omega_r \gg \gamma$ .

## 452 Growth Rate of Lower Hybrid Waves in a Homogeneous Plasma

453 To estimate the growth rate of the lower hybrid waves in a homogeneous plasma,  
 454 we include the complex frequency  $\omega = \omega_r + i\gamma$  in the expression derived previously for  
 455 the dielectric tensor and solve for  $\gamma$ , by setting  $Im(K) = 0$  and assuming that  $\gamma \ll$   
 456  $\omega_r$ .

457 We first note that  $\Theta'_e \gg 1$ , allowing us to drop the term  $i\sqrt{\pi}e^{-\Theta'^2_e}$  from the elec-  
 458 tron plasma dispersion function  $Z(\Theta'_e)$ . In the case of ions, at the altitudes, times and

459 frequencies considered,  $\theta_i \approx 7 - 8$ , indicating that the exponential term must be re-  
 460 tained. In addition,  $\frac{k^2 v_{te}^2}{\Omega_e^2} \ll 1$ , justifies the use of  $\Lambda_0(\eta^2) \approx 1$ . Starting with equa-  
 461 tion 2, for a single ion species:

$$\begin{aligned} Im(K) &= \frac{1}{k^2 \lambda_{de}^2} \Lambda_0(\eta^2) Im[(\Theta'_e) Z(\Theta'_e)] + \frac{1}{k^2 \lambda_{d\alpha}^2} Im[(\theta_\alpha) Z(\theta_\alpha)] \\ &\approx \frac{\omega_{pe}^2}{k^2 v_{te}^2} \left[ \left( 1 - \frac{k^2 v_{te}^2}{\Omega_e^2} + \dots \right) \left( \sqrt{\pi} Im(\Theta'_e e^{-\Theta'_e^2}) + \frac{\Theta'_{ei}}{\Theta'_{er}^3} + 3 \frac{\Theta'_{ei}}{\Theta'_{er}^5} + \dots \right) \right] \\ &+ \frac{\omega_{p\alpha}^2}{k^2 v_{t\alpha}^2} \left( \sqrt{\pi} Im(\theta_\alpha e^{-\theta_\alpha^2}) + \frac{\theta_{\alpha i}}{\theta_{\alpha r}^3} + 3 \frac{\theta_{\alpha i}}{\theta_{\alpha r}^5} + \dots \right) \\ &\approx \frac{\omega_{pe}^2}{k^2 v_{te}^2} \left[ \left( \frac{\Theta'_{ei}}{\Theta'_{er}^3} + 3 \frac{\Theta'_{ei}}{\Theta'_{er}^5} + \dots \right) \right] + \frac{\omega_{p\alpha}^2}{k^2 v_{t\alpha}^2} \left( \sqrt{\pi} Im(\theta_\alpha e^{-\theta_\alpha^2}) + \frac{\theta_{\alpha i}}{\theta_{\alpha r}^3} + 3 \frac{\theta_{\alpha i}}{\theta_{\alpha r}^5} + \dots \right) \end{aligned}$$

462 Setting  $Im(K) = 0$ , dividing by  $\frac{\omega_{p\alpha}^2}{k^2 v_{t\alpha}^2}$ , taking into account  $\gamma \ll \omega_r$  and  $\Theta'_e \gg 1$ ,  
 463 the equation can be recast as:

$$\begin{aligned} 0 &\approx \frac{T_i}{T_e} \left( \frac{\Theta'_{ei}}{\Theta'_{er}^3} \right) + \left( \sqrt{\pi} \theta_{\alpha r} Re(e^{-\theta_\alpha^2}) + \frac{\theta_{\alpha i}}{\theta_{\alpha r}^3} + 3 \frac{\theta_{\alpha i}}{\theta_{\alpha r}^5} + \dots \right) \\ &\approx -\sqrt{\pi} Re \left( e^{-\theta_{\alpha r}^2 - 2i\theta_{\alpha r}\theta_{\alpha i}} \right) + \frac{\gamma}{\omega_r^3} 2k^2 \left[ \frac{T_i}{T_e} \cos^2(\beta) v_{te}^2 - v_{t\alpha}^2 \left( 1 + \frac{3}{\omega_r^2} \right) \right] \\ &\approx -\sqrt{\pi} \omega_r^3 (e^{-\theta_{\alpha r}^2}) \cos(-2\theta_{\alpha r}\theta_{\alpha i}) + \gamma 2k^2 \left[ \frac{T_i}{T_e} (\cos^2(\beta) v_{te}^2) - v_{t\alpha}^2 \right] \end{aligned}$$

464 where we replaced the normalized velocities by  $\Theta'_{ei} = \frac{\gamma}{k \cos(\beta) \sqrt{2} v_{te}}$  and  $\theta'_{\alpha i} = \frac{\gamma}{k \sqrt{2} v_{t\alpha}}$   
 465 except for the exponential terms, and ignored the term  $\frac{3}{\omega_r^2}$  since it is  $\ll 1$ . Since  $\gamma$  can-  
 466 not be factored from the cosine term above, we will leave it on the right side of the equa-  
 467 tion to obtain:

$$\gamma \approx \frac{\omega_r^3 \sqrt{\pi} (e^{-\theta_{\alpha r}^2}) \cos(-2\theta_{\alpha r}\theta_{\alpha i})}{\left( \frac{T_i}{T_e} (2k^2 \cos^2(\beta) v_{te}^2) - 2k^2 v_{t\alpha}^2 \right)}$$

468 When we consider  $\beta \approx 90^\circ$ , and values of  $\frac{\theta_{\alpha i}}{\theta_{\alpha r}} \ll 0.1\%$ , which was verified numeri-  
 469 cally for  $k < 6$ ,  $\cos(-2\theta_{\alpha r}\theta_{\alpha i}) \approx 1$  and the expression simplifies to:

$$\gamma \approx \frac{-(\omega_r - \mathbf{k} \cdot \mathbf{u}_i)^3 \sqrt{\pi} (e^{-\theta_{\alpha r}^2})}{2k^2 v_{t\alpha}^2} \quad (5)$$

470 where a drift  $\mathbf{u}_i$  was included.

## 471 References

472 Andreev, N. E. (1971). Parametric plasma instability in constant magnetic and  
 473 weak high-frequency electric fields. *Izvestiya Vysshikh Uchebnykh Zavedenii, Radiofizika*, 14(8), 1160 - 1167.

474 Azarenkov, N. A., & Chibisov, D. (2019). High-frequency oscillations in plasma of  
 475 lower hybrid cavities. *BAHT. 2019.*, 122, 24-26.

475 Balsley, B. B. (1964). Evidence of a stratified echoing region at 150 kilometers in the  
476 vicinity of the magnetic equator during daylight hours. *J. Geophys. Res.*, 69,  
477 1925-1930.

478 Bell, T. F., & Ngo, H. D. (1988). Electrostatic waves stimulated by coherent VLF  
479 signals propagating in and near the inner radiation belt. *J. Geophys. Res.*,  
480 93(A4), 2599-2618.

481 Bell, T. F., & Ngo, H. D. (1990). Electrostatic lower hybrid waves excited by elec-  
482 tromagnetic whistler mode waves scattering from planar magnetic field aligned  
483 plasma density irregularities. *J. Geophys. Res.*, 95(A1), 149-172.

484 Berger, R. L., & Perkins, F. W. (1976). Thresholds of parametric instabilities near  
485 the lower-hybrid frequency. *Phys. Fluids*, 19(3), 406-411.

486 Berthelier, J. J., Malingre, M., Pfaff, R., Seran, E., Pottelette, R., Jasperse, J., ...  
487 Parrot, M. (2008). Lightning-induced plasma turbulence and ion heating in  
488 equatorial ionospheric depletions. *Nature Geosci.*, 1, 101-105.

489 Bonnell, J. W., Schuck, P. W., Pinçon, J.-L., Seyler, C. E., & Kintner, P. M. (1998).  
490 Observation of bound states and counter-rotating eigenmodes in the auroral  
491 ionosphere. *Phys. Rev. Lett.*, 80(26), 5734-5737.

492 Booker, H. G., & Wells, H. W. (1938). Scattering of radio waves by the F region of  
493 the ionosphere. *J. Geophys. Res.*, 35(4), 249-256.

494 Buneman, O. (1963). Excitation of field aligned sound waves by electron streams.  
495 *Phys. Rev. Lett.*, 10, 285-287.

496 Chang, T. (1993). Lower-hybrid collapse, caviton turbulence, and charged particle  
497 energization in the topside auroral ionosphere and magnetosphere. *Phys. Flu-  
498 ids B*, 5(7), 2646 - 2656.

499 Chau, J. L., & Kudeki, E. (2006). Statistics of 150-km echoes over jicamarca based  
500 on low-power VHF observations. *Ann. Geophys.*, 24(5), 1305 - 1310.

501 Chau, J. L., & Kudeki, E. (2013). Discovery of two distinct types of equatorial 150  
502 km radar echoes. *Geophys. Res. Lett.*, 40, 4509 - 4514.

503 Chibisov, D. V., & Mikhailenko, V. (2013). The lower hybrid waves driven by inho-  
504 mogeneous ion-ring distribution. *Problems of Atomic Science and Technology,  
505 Series Plasma Physics*, 6, 99 -101.

506 Doolen, G. D., DuBois, D. F., & Rose, H. A. (1996). Nucleation of cavitons in  
507 strong langmuir turbulence. *Phys. Rev. Lett.*, 54(8), 804 - 807.

508 Dovner, P. O., Eriksson, A. I., Boström, R., & Holback, B. (1994). Freja multiprobe  
 509 observations of electrostatic solitary structures. *Geophys. Res. Lett.*, *21*(27),  
 510 1827 - 1834.

511 Dovner, P. O., Eriksson, A. I., Boström, R., & Holback, B. (1997). The occurrence  
 512 of lower hybrid cavities in the upper ionosphere. *Neuroscience*, *24*(5), 619 -  
 513 622.

514 Farley, D., Balsley, B. B., Woodman, R., & McClure, J. (1970). Equatorial spread F:  
 515 implications of VHF radar observations. *J. Geophys. Res.*, *75*, 7199.

516 Farley, D. T. (1963). A plasma instability resulting in field-aligned irregularities in  
 517 the ionosphere. *Proc. R. Soc., London Ser. A*, *68*, 6083.

518 Farley, D. T. (1969). Incoherent scatter correlation function measurements. *Radio  
 519 Science*, *4*(10), 935-963.

520 Farley, D. T., Dougherty, J. P., & Barron, D. W. (1961). Scattering in a magnetic  
 521 field. *Proc. R. Soc., London Ser. A*, *263*, 238 - 258.

522 Forbes, J. (1981). The equatorial electrojet. *Rev. of Geophys.*, *19*, 469.

523 Huba, J. D. (1981a). Diffusion of small-scale density irregularities during equatorial  
 524 spread F. *J. Geophys. Res.*, *7*(7), 9107 - 9114.

525 Huba, J. D., Joyce, G., & Feder, J. A. (2000). Sami2 is another model of the  
 526 ionosphere (SAMI2): A new low-latitude ionosphere model. *Journal of Atmo-  
 527 spheric and Terrestrial Physics*, *105*(A10), 23035 - 23053.

528 Huba, J. D., & Ossakow, S. L. (1979). On the generation of 3-m irregularities during  
 529 equatorial spread F by low-frequency drift waves. *J. Geophys. Res.*, *84*, 6697.

530 Huba, J. D., & Ossakow, S. L. (1981). Physical mechanism of the lower-hybrid-  
 531 drift instability in a collisional plasma. *Journal of Atmospheric and Terrestrial  
 532 Physics*, *43*(8), 775-778.

533 Huba, J. D., & Ossakow, S. L. (2000). An overview and synthesis of plasma irreg-  
 534 ularities in equatorial spread F. *Journal of Atmospheric and Solar-Terrestrial  
 535 Physics*, *62*, 1037 - 1056.

536 Hysell, D. L., & Chau, J. L. (2006). Optimal aperture synthesis radar imaging. *Ra-  
 537 dio Sci.*, *41*, RS2003.

538 Hysell, D. L., Jafari, R., Milla, M. A., & Meriwether, J. W. (2014). Data-driven nu-  
 539 matical simulations of equatorial spread F in the peruvian sector. *J. Geophys.  
 540 Res. Space Physics*, *119*, 3815 - 3827.

541 Hysell, D. L., Milla, M. A., & Woodman, R. F. (2017). Data-driven numerical simu-  
 542 lations of equatorial spread F in the Peruvian sector. *J. Geophys. Res.*, *122*(2),  
 543 2292 - 2299.

544 Hysell, D. L., Vierinen, J., & Sultzer, M. P. (2017). On the theory of the incoherent  
 545 scatter gyrolines. *Radio Sci.*, *52*, 723 - 730.

546 Hysell, D. L., Vierinen, J., & Sultzer, M. P. (2019). The case for combining a large  
 547 low-band very high frequency transmitter with multiple receiving arrays for  
 548 geospace research: A geospace radar. *Radio Sci.*, *54*(7), 533 - 551.

549 Høymark, S., Pécseli, H. L., Lybekk, B., Trulsen, J., & Eriksson, A. (2000). The  
 550 equatorial electrojet. *J. Geophys. Res.*, *105*(A8), 18519 - 18535.

551 Inan, U. S., & Bell, T. F. (1985). Spectral broadening of VLF transmitter signals  
 552 observed on DEI: a quasi-electrostatic phenomenon? *J. Geophys. Res.*, *90*,  
 553 1771.

554 Kaw, P. (1976). Parametric excitation of electrostatic waves in magnetized plasmas.  
 555 *Adv. Plasma Phys.*, *6*, 207 - 236.

556 Kintner, P. M., Vago, J., Chesney, S., Arnoldy, R. L., Lynch, K. A., Pollock, C. J.,  
 557 & Moore, T. E. (1992). Localized lower hybrid acceleration of ionospheric  
 558 plasma. *Phys. Rev. Lett.*, *68*(16), 2448 - 2451.

559 Kjus, S. H., Pécseli, H. L., Lybekk, B., Holtet, J., Trulsen, J., Lür, H., & Eriksson,  
 560 A. (1998). Statistics of the lower hybrid wave cavities detected by the freja  
 561 satellite. *J. Geophys. Res.*, *103*(A11), 26633 - 26647.

562 Knudsen, D. J., Wallis, D. D., & James, H. G. (1998). ELF/VLF structures ob-  
 563 served by OEDIPUS C. *presented at the Int. Radio Science Meeting, Jan.*  
 564 *5-8*.

565 Kudeki, E., & Fawcett, C. D. (1993). High resolution observations of 150 km echoes  
 566 at jicamarca. *J. Geophys. Res.*, *20*(18), 1987-1990.

567 LaBelle, J., Kintner, P. M., Yau, A. W., & Whalen, B. A. (1986). Large amplitude  
 568 wave packets observed in the ionosphere in association with transverse ion  
 569 acceleration. *J. Geophys. Res.*, *91*(A6), 7113 - 7118.

570 Lee, M. C., & Kuo, S. P. (1984). Production of lower hybrid waves and field-aligned  
 571 plasma density striations by whistlers. *J. Geophys. Res.*, *89*, 10873.

572 Lehmacher, G. A., Wu, H., Kudeki, E., Reyes, P., Hysell, D. L., & Milla, M. (2020).  
 573 Height variation of gaps in 150-km echoes and whole atmosphere community

574 climate model electron densities suggest link to upper hybrid resonance. J.  
 575 *Geophys. Res.*, 125.

576 Longley, W. J., Oppenheim, M. M., Pedatella, N. M., & Dimant, Y. S. (2020). The  
 577 photoelectron-driven upper hybrid instability as the cause of 150-km echoes.  
 578 *Geophys. Res. Lett.*, 47(8), 1-10.

579 Lynch, K. A., Arnoldy, R. L., Kintner, P., Schuck, P., Bonnell, J., & Coffey, V.  
 580 (1999). Auroral ion acceleration from lower hybrid solitary structures: A sum-  
 581 mary of sounding rocket observations. *J. Geophys. Res.*, 104(A12), 28515 -  
 582 28534.

583 Lynch, K. A., Arnoldy, R. L., Kintner, P. M., & Bonnell, J. (1996). The AMI-  
 584 CIST auroral sounding rocket—a comparison of transverse ion acceleration  
 585 mechanisms. *Geophys. Res. Lett.*, 23(8), 3293 - 3296.

586 Malingre, M., Berthelier, J.-J., Pfaff, R., Jasperse, J., & Parrot, M. (2008).  
 587 Lightning-induced lower-hybrid turbulence and trapped extremely low fre-  
 588 quency (ELF) electromagnetic waves observed in deep equatorial plasma den-  
 589 sity depletions during intense magnetic storms. *J. Geophys. Res.*, 113(A11),  
 590 1-17.

591 McAdams, K. L., Labelle, J., Schuck, P. W., & Kintner, P. M. (1998). PHAZE ii  
 592 observations of lower hybrid burst structures occurring on density gradients.  
 593 *Geophys. Res. Lett.*, 25(16), 3091 - 3094.

594 Morgan, M. G. (1979). Equatorial hiss in the topside ionosphere. *J. Geophys. Res.*,  
 595 84(A12), 7279 - 7287.

596 Musher, S. L., & Sturman, B. I. (1975a). Collapse of plasma waves near the lower  
 597 hybrid resonance. *Pis'ma Zh. Eksp. Teor. Fiz.*, 22(11), 537 - 542.

598 Musher, S. L., & Sturman, B. I. (1975b). Collapse of plasma waves near the lower  
 599 hybrid resonance. *JETP Lett.*, 22(11), 265 - 267.

600 Pinçon, J., L., Kintner, P. M., Schuck, P., & Seyler, C. E. (1997). Observation and  
 601 analysis of lower hybrid solitary structures as rotating eigenmodes. *J. Geophys.  
 602 Res.*, 102(8), 17283 - 17296.

603 Pécseli, H. L., Iranpour, K., Holter, O., Lybekk, B., Holtet, J., Trulsen, J., ... Hol-  
 604 back, B. (1996). Lower-hybrid wave cavities detected by the Freja-satellite. *J.  
 605 Geophys. Res.*, 101(8), 5299.

606 Pécseli, H. L., Lybekk, B., Trulsen, J., & Eriksson, A. (1997). Lower-hybrid wave

607        cavities detected by the Freja-satellite. *Plasma Phys. Control. Fusion*, 39(5A),  
608        227 - 236.

609        Rastogi, P. K., & Bowhill, S. A. (1976). Scattering of radio waves from the  
610        mesosphere-2. evidence for intermittent mesospheric turbulence. *Journal of*  
611        *Atmospheric and Terrestrial Physics*, 38(5), 449- 468.

612        Robinson, P. A. (1996). Scalings, spectra, and statistics of strong wave turbulence.  
613        *Phys. Plasmas*, 3(1), 192 - 201.

614        Robinson, P. A. (1999). Nonlinear lower hybrid solitary structures in auroral plas-  
615        mas: comparison of theory with observations. *Adv. Space Res.*, 23(10), 1679 -  
616        1688.

617        Rogister, A., & D'Angelo, N. (1970). Type2 irregularities in the equatorial electro-  
618        jet. *J.Geophys Res.*, 75(19), 3879 - 3887.

619        Sanbonmatsu, K., Goldman, M. V., & Newman, D. L. (1995). Nonlinear coupling of  
620        lower hybrid waves to the kinetic low-frequency plasma response in the auroral  
621        ionosphere. *Geophys. Res. Lett.*, 20(17), 2397 - 2400.

622        Schuck, P., Bonnell, J., & Kintner, P. (2003). A review of lower hybrid solitary  
623        structures. *IEEE Trans. Plasma Sci.*, 31, 1125 - 1176.

624        Schuck, P., Seyler, C. E., Pinçon, J.-L., Bonnell, J. W., & Kintner, P. M. (1998).  
625        Theory simulation and observation of bound states associated with lower hy-  
626        brid solitary structures. *J. Geophys. Res.*, 103(A4), 6935 - 6953.

627        Schuck, P. W., Ganguli, G. I., & Kintner, P. M. (2002). On the role of lower hybrid  
628        collapse in the auroral ionosphere. *Phys. Rev. Lett.*, 89(6), 065 002.

629        Schuck, P. W., & Seyler, C. E. (1999a). Lower hybrid solitary structures: electro-  
630        magnetic and electrostatic scattering and mode conversion. *Eos Trans. AGU*,  
631        17.

632        Schuck, P. W., & Seyler, C. E. (1999b). Lower hybrid solitary structures: Resonant  
633        scattering from preexisting density depletions. *Eos Trans. AGU*, 80(46).

634        Seyler, C. (1994). Lower hybrid wave phenomena associated with density depletions.  
635        *J. Geophys. Res.*, 99(A10), 19 513-19 525.

636        Shapiro, V., Shevchenko, V. I., Solov'ev, G. I., Kalinin, V. P., R.Bingham, Sagdeev,  
637        R. Z., ... Su, J. J. (1993). Wave collapse at the lower hybrid resonance. *Phys.*  
638        *Fluids B*, 5(9), 3148 - 3162.

639        Shapiro, V. D. (1998). Modulational interaction of the lower hybrid waves with a

